Received: 7 June 2023 | Accepted: 30 August 2023

DOI: 10.1002/vzj2.20286

Vadose Zone Journal

ORIGINAL ARTICLE

Heat transport from atmosphere through the subsurface to drinking-water supply pipes

Elisabeth Nissler[1] | **Samuel Scherrer**[1] | **Holger Class**[1] | **Tanja Müller**[2] | **Mark Hermannspan**[2] | **Esad Osmancevic**[2] | **Claus Haslauer**[1]

[1]Institute for Modelling Hydraulic and Environmental Systems, University of Stuttgart, Stuttgart, Germany

[2]RBS Wave GmbH, Stuttgart, Germany

Correspondence
Claus Haslauer, University of Stuttgart, Institute for Modelling Hydraulic and Environmental Systems, Pfaffenwaldring 61, 70569 Stuttgart, Germany.
Email: claus.haslauer@iws.uni-stuttgart.de

Assigned to Associate Editor Jingfeng Wang.

Abstract

Drinking-water quality in supply pipe networks can be negatively affected by high temperatures during hot summer months due to detrimental bacteria encountering ideal conditions for growth. Thus, water suppliers are interested in estimating the temperature in their distribution networks. We investigate both experimentally and by numerical simulation the heat and water transport from ground surface into the subsurface, (i.e., above drinking-water pipes). We consider the meteorological forcing functions by a sophisticated approach to model the boundary conditions for the heat balance at the soil–atmosphere interface. From August to December 2020, soil temperatures and soil moisture were measured dependent on soil type, land-use cover, and weather data at a pilot site, constructed specifically for this purpose at the University of Stuttgart with polyethylene and cast-iron pipes installed under typical in situ conditions. We included this interface condition at the atmosphere–subsurface boundary into an integrated non-isothermal, variably saturated (Richards') the numerical simulator DuMu^x 3. This allowed, after calibration, to match measured soil temperatures with ±2°C accuracy. The land-use cover influenced the soil temperature in 1.5 m more than the soil material used for back-filling the trench above the pipe.

1 | INTRODUCTION

In recent years, unusually warm water in drinking-water supply pipes has been observed and suspected to be caused by high air temperatures during the summers (Osmancevic & Hüsam, 2021). Such conditions pose a threat to drinking-water quality as elevated temperatures can lead to increased and undesired microbial activity and, hence, to deteriorated drinking-water quality. It is feared that this situation will worsen with climate change. Therefore, detailed knowledge on the influence of soil and recharge temperatures is needed for being able to estimate the temperature in the water of distribution networks.

Generally, higher soil temperatures over the last decades are confirmed (e.g., Chen et al., 2021) and have various effects on microbiological and chemical processes as well as on vegetation periods that vary with time. Therefore, there are several approaches to determine soil temperatures with simple models, validated for special regions. Sharma et al. (2010) were predicting soil temperatures up to 0.5 m, based on air temperature, using linear regression in Southern Mexico. Horton Brian (2011) worked with a coefficient model, based

on rainfall and air temperature, covering entire Australia. Jungqvist et al. (2014) were interested in Swedish forests and worked with climate models. Rankinen et al. (2004) proposed a model, working with regional soil and climate parameters, predicting soil temperatures between 20 and 50 cm, interested on snow-covered soils.

Various codes to calculate water saturations are available, which are all based on solving Richards' equation, with different priorities. Simunek and Bradford (2008) give an overview of various simulation codes available, namely HYDRUS, MODFLOW-SURFACT, STOMP, SWAP, TOUGH2, and VS2DI. HYDRUS is commonly used for variably saturated non-isothermal conditions, for example, Steenpass et al. (2010). Guo et al. (2017) use PCSiWaPro to predict seepage and concentration of pollutants. The tool WASIM is often used to describe catchments, as for example in Burkina Faso (Idrissou et al., 2020), where a successful validation was performed.

There are many topics, related to soil temperature and saturation, such as drainage in cyclic loading (Komolvilas & Kikumoto, 2017) or the influence of groundwater temperature on river temperature (Kurylyk et al., 2015). Kelleners et al. (2016) worked on water flow in variably saturated soils, taking into account snow. Herrada et al. (2014) proposed a model to predict infiltration rates. Corona and Ge (2022) were focusing on high intensity precipitation events. Tran et al. (2016) showed that taking heat transport into account yields better results for an inversion scheme to define soil parameters. Sandor and Fodor (2012) demonstrated the relevance of a good vegetation model to quantify root uptake. Wessolek et al. (2022) focused on heat transport and worked with earth cables as heat sources.

Literature shows various approaches to describe the temperature evolution in soils forced from the atmosphere together with water flow. One approach is to reconstruct the soil thermal field from a single measurement, which was developed and validated by Wang (2012). Another approach, one that we are also following, is to solve the energy balance at the surface, which needs expressions for evapotranspiration and sensible heat flow. This is, for example, done in Saito et al. (2006) within the simulator HYDRUS, where evaporation is set as boundary condition (Bittelli et al., 2008) and evaporation is part of the solution.

This study uses an approach similar to HYDRUS, calculating sensible heat flow based on the Penman–Monteith equation (Allen et al., 1998) by using adequate measurements of meteorological data. The evaporation is then calculated from the latent heat flow, using the Bowen ratio, as described in Section 2.2.6. The goal of this study is to implement this kind of boundary condition in an open-access code, to calibrate against longer time series, and finally to obtain time series of the temperature of groundwater recharge which in this case improve the management of drinking-water networks during changing climatic conditions.

Core Ideas

- We measure and model the temperature of groundwater recharge.
- We solve the heat and water balance at the atmosphere–subsurface interface.
- Data: time series of hydrometeorological parameters, hydraulic, and thermal material properties.
- Goal: estimate temperatures relevant for buried drinking-water supply pipes.

We modeled the influence of the meteorological forcing functions, the soil structure, and the land-use cover on temperatures between ground surface and the subsurface. At a pilot site, we focus with our analysis up to a depth of 1.5 m, that is, a typical laying depth for drinking-water pipes in Germany. While applied to drinking-water supply pipes, this work is of general relevance as it describes and models the temperature of groundwater recharge driven by meteorological forcing functions. This temperature distribution and its evolution with climate change are critical for resilient urban infrastructure.

A pilot site at the University of Stuttgart has been constructed, where drinking-water pipes of PE and cast iron were installed at a depth of 1.50 m over a horizontal stretch of 15 m. The trench was back-filled with two different materials: gravelly material typical for conditions when pipes are buried below streets and the naturally occurring silty clay. Two different types of land cover, natural vegetation and asphalt, have been placed on the surface. The subsurface has been instrumented with 64 temperature sensors, 8 soil moisture sensors, and detailed hydrometeorological observations are available from the neighboring University of Stuttgart's weather station. In addition to the measurements, we adapted and employed a numerical simulator for estimating both soil temperatures and moisture contents. The study aimed at including the incorporation of the meteorological forcing and the variable saturation conditions.

Section 2 describes the test site and the numerical simulation methods, starting with a description of the pilot site. Furthermore, this section introduces the numerical model and the novel approach chosen to implement the conditions at the air–subsurface interface. The results section (Section 3) presents the comparison between measured data and numerical simulations with a calibrated set of parameters. The results are discussed in Section 4, followed by the conclusions (Section 5).

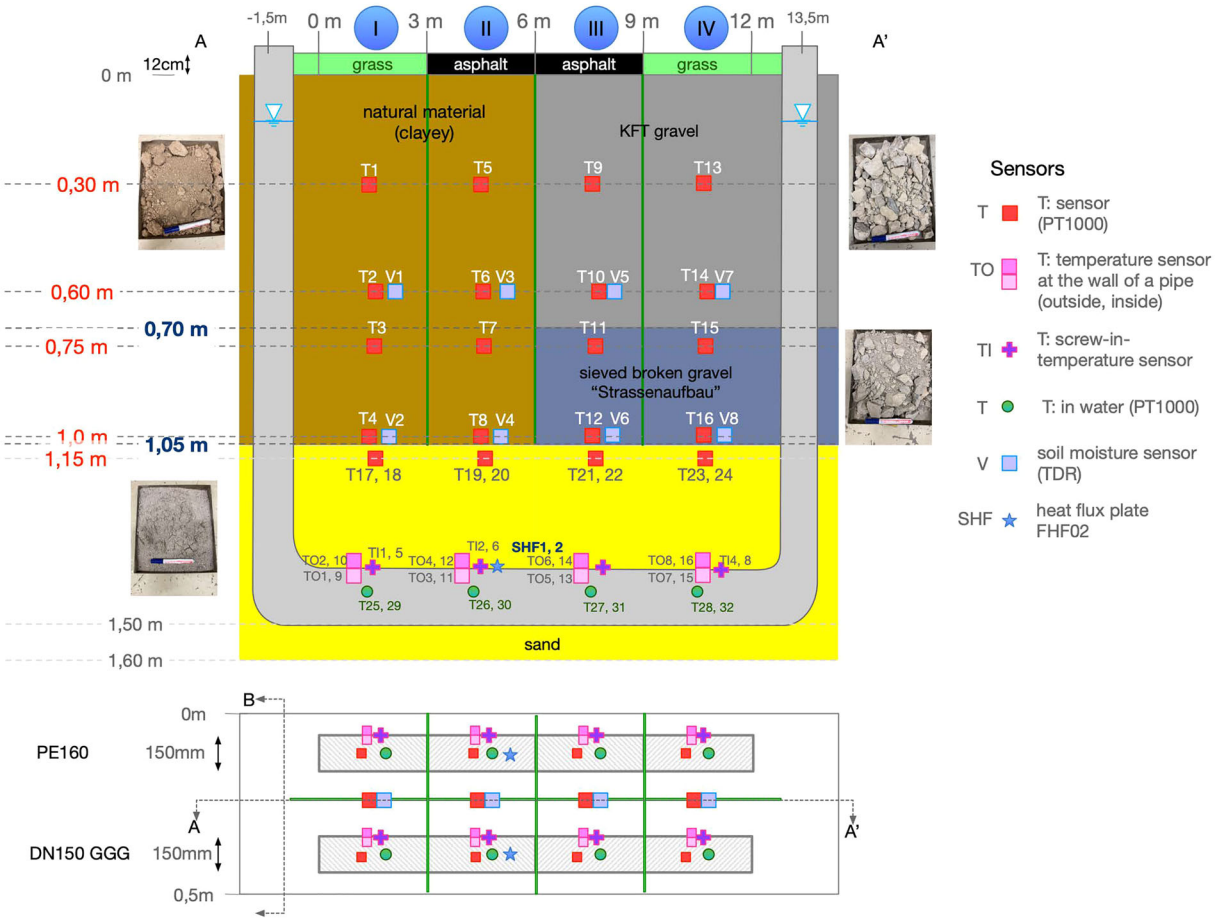

FIGURE 1 Setup of the pilot site.

2 | MATERIALS AND METHODS

This section provides a description of the pilot site, then the numerical model is introduced. A particular emphasis is put on the adaption of the model to be capable of including the meteorological forcing functions in the heat and mass balances.

2.1 | The experimental pilot site

Two pipes typical for drinking-water supply in terms of dimension (inner diameter: 150 mm) and material (PE and cast iron) were laid into a 1.50 m deep, 15 m long, and ≈1 m wide trench (Figure S1). The pipe was set on a slight angle into beach sand with a horizontal length of 12 m, Figure 1 shows the dimensions. At both ends of the pipes, vertical extensions above ground surface were constructed. The trench was backfilled with two types of porous media, (a) a silty clay, the naturally occurring material at the site and (b) gravelly material typical for street construction ("KFT gravel" and "sieved broken gravel"). The pipes were filled with drinking water. On the ground surface, two ≈12 cm thick layers of different land-use were established, (a) the naturally occurring vegetation ("grass") and (b) asphalt. Thus, in total, four combinations of porous media and land-use were replicated, the stations referenced by Roman numerals. Each station was insulated against thermal influences from the neighboring sites.

The trench was installed in direct vicinity to (https://lhg-902.iws.uni-stuttgart.de) the weather station of the University of Stuttgart, where the following hydro-meteorological variables are measured:

- long wave radiation incoming
- short wave radiation incoming
- air temperature in 2 m above ground
- wind velocity in 2 m above ground
- relative humidity in 2m above ground
- precipitation intensity

At the site, a stationary phreatic water table at a depth of ~5.1 m below ground surface has been observed, sitting on top of a local low-conductive layer ("Arietenkalk"). Atmospheric pressure was set constant to a value of 101,325 Pa, as its influence on vapor pressure was considered negligible.

The variables soil temperature and soil moisture were observed with 64 sensors (24 temperature sensors in the porous media, 16 temperature sensors in each pipe, 8 soil moisture sensors) with the aim to monitor the evolution of temperature and soil moisture from the ground surface toward the water pipes. Temperatures were measured using PT1000 sensors, soil moistures using "Teros 10" sensors from the metergroup. Time series of all variables were recorded in 5 min intervals, backed up, and stored in a hdf5 file using python (Virtanen et al., 2020) for data processing.

The observed data will be compared to numerical simulation results obtained by including meteorological forcing functions at the ground surface on both heat and water balances.

2.2 | The numerical model

2.2.1 | Balance equations

The modeling of heat transport in a partially water saturated porous medium requires solving the coupled balances for water and heat. Our system of interest is located in the variably saturated zone, where the water balance can be formulated in terms of the Richards' equation, which can be considered as a simplified version of the multiphase flow equation under the assumption of an infinitely mobile gas phase. Richards' equation combines the multiphase version of Darcy's law with the continuity equation for water, thus taking into account the effects of capillary pressure and relative permeability:

$$\frac{\partial\, \phi S_{\mathrm{w}} \varrho_{\mathrm{w}}}{\partial t} - \nabla \left\{ \varrho_{\mathrm{w}} \frac{k_{\mathrm{rw}}}{\mu_{\mathrm{w}}} \mathbf{K} \left(\nabla p_{\mathrm{w}} - \varrho_{\mathrm{w}} \mathbf{g} \right) \right\} = q_{\mathrm{w}} \,, \qquad (1)$$

where S is the saturation, ϕ the porosity, ϱ the density, μ the dynamic viscosity, k_{r} the relative permeability as a function of saturation, p the pressure, q_{w} the source term for water, and K the hydraulic conductivity tensor. The index w denotes water. The Richards' model assumes that the pressure of the gas phase is constant, that is, in our setting at atmospheric conditions, 1 bar. The pressure of the water phase depends on the water saturation via the capillary-pressure-saturation relationship as will be detailed further below.

Assuming thermal equilibrium between solid and fluids, the heat balance coupled to the Richards' equation can be written as follows:

$$\phi \frac{\partial(\rho_{\mathrm{w}} u_{\mathrm{w}} S_{\mathrm{w}})}{\partial t} + (1-\phi) \frac{\partial(\rho_{\mathrm{s}} c_{\mathrm{s}} T)}{\partial t} + \nabla \cdot \left(\rho_{\mathrm{w}} h_{\mathrm{w}} \mathbf{v}_{\mathrm{w}} - \lambda \nabla T \right) = q_{\mathrm{h}}. \qquad (2)$$

Here, u_{w} is the specific internal energy of the water phase, c_{s} is the specific heat capacity of the solid, h the specific enthalpy, λ represents the averaged heat conductivity of the fluid-filled porous medium, v_{w} is the velocity of the water phase, which is obtained from Darcy's law as it is already implicitly inserted in Equation (1), T is the temperature, and q_{h} the source term for heat.

2.2.2 | Numerical simulation platform

For numerical implementation, we were working with DuMu$^{\mathrm{x}}$ 3 (Koch et al., 2020; Scheer et al., 2020), an open-source simulator and research code for flow and transport in porous media. With its modular design, DuMu$^{\mathrm{x}}$ allows for a flexible choice of physics and discretization methods and solution algorithms, and it facilitates the implementation of new approaches and adaption as in this study. For spatial discretization, we used the Box method for this study; for details, we refer to Scheer et al. (2020). The Box method employs a finite element mesh containing the nodes at which the solution is calculated, while there is a secondary mesh constructed, on which a finite-volume scheme is used. Thus, the Box method guarantees local mass conservation.

2.2.3 | Hydraulic properties

Richards' equation describes water flow in partially saturated porous media. Thus, the gas phase is present, though not explicitly modeled. Using the Richards' approach of multiphase flow in the variably saturated zone implies that the relative permeability of the water phase as a function of water saturation is considered as well as the capillary pressure also dependent on water saturation. We aim to reduce the overall uncertainty by measuring relevant parameters (saturated hydraulic conductivity, relationship between capillary pressure and saturation). In situations where measurements are difficult, for example, because of large grain sizes such as in the gravel for this study, the uncertainty due to the parameterisation is considered minor compared to the uncertainty of the overall behavior. For the variably saturated relationships, several models exist in addition to the van Genuchten parameterisation, for example, Brooks and Corey (1966) or Clapp and Hornberger (1978). Working with a different approach can lead to different results, as demonstrated in Yang and Wang (2014). We compared parameters of a Brook–Corey model to van Genuchten's model and saw similar results for both models but a better stability for van Genuchten's model. For this reason, in this study, the relative-permeability-saturation relationship as well as the capillary-pressure-saturation relationship were used according to van Genuchten's model. It

can be written for the capillary pressure as:

$$p_c = \frac{1}{\alpha}\left(S_e^{-1/m} - 1\right)^{1/n} \tag{3}$$

with the effective saturation

$$S_e = \frac{S_w - S_{wr}}{1 - S_{wr}}\,. \tag{4}$$

α [1/Pa] and n are parameters to be determined specifically for the porous material. α is a scaling parameter for the magnitude of the capillary pressure (comparable to the entry pressure in Brooks–Corey's approach), and the parameter n characterizes the uniformity or non-uniformity of the pore-size distribution. A large n expresses a comparatively uniform soil. Commonly, the parameter m is expressed in terms of n by

$$m = 1 - \frac{1}{n}\,. \tag{5}$$

The relative-permeability function is, accordingly:

$$k_{rw} = \sqrt{S_e}\left[1 - \left(1 - S_e^{1/m}\right)^m\right]^2. \tag{6}$$

We measured α, n, and saturated conductivity for the natural material with the simplified evaporation method as described in Peters and Durner (2008) with a HYPROP device. This method was not suitable for the sandy gravel, as these materials are too coarse for measurements, hence their parameters were calibrated. Asphalt is basically not permeable, thus should receive a close-to-zero permeability. However, in our case, the 1D simplification of the model domain cannot account for effects that occur close to the surface and lead to small lateral inflow of water, which contradicts the idealized 1D assumption of an impermeable boundary. Thus, the apparent permeability of the asphalt in the simplified 1D system is part of the calibration procedure. For the grass surface, it is difficult to perform representative measurements. Consequently, all permeabilities were used as calibration parameters. Another key hydraulic property is the porosity. Again, this could be measured for some soils (e.g., sand), for others, (e.g., grass) it would have been difficult to measure. For this reason, properties were also used as calibration parameters.

2.2.4 | Thermal properties

Basically, the thermal conductivity and the heat capacity are material- and temperature-dependent properties of the porous medium. While temperature dependence is small in the range of temperatures encountered in our application (-10 to 40°C), water content plays a more important role. In reality, we have an inhomogeneous mixture of soil, water, and air. Thus, the water saturation has an effect on the thermal properties. It is challenging to find an appropriate model or a set of tabulated values for a given material. There are several models available to calculate thermal conductivity based on water content, for example, Ghanbarian and Daigle (2015); Lu et al. (2007); Lu and Dong (2015); Markert et al. (2017); Sadeghi et al. (2018).

The effective heat capacity can be computed as the volumetric average of water, air, and solid heat capacity. The effective thermal conductivity of a wet solid matrix with a given water content depends on the grain sizes. Johansen (1975) introduced a way to determine the effective thermal conductivity by defining the effective thermal conductivity and using K_e, the Kersten number:

$$\lambda_{eff} = \lambda_{dry} + K_e(S_w)\left(\lambda_{wet} - \lambda_{dry}\right). \tag{7}$$

Thus, the effective conductivity is calculated from the values for the dry conductivity and the wet conductivity. There are several models available based on measured correlations (e.g., Somerton et al., 1974). For this research, we were working with Lu et al. (2007), as the temperatures and soils used for the underlying correlation fit to our test settings. In their approach, the definition for K_e is

$$K_e(S_w) = \exp\alpha_{Lu}\left[1 - S^w_{(\alpha_{Lu}-1.33)}\right], \tag{8}$$

and the dry conductivity is calculated as

$$\lambda_{dry} = -a \cdot \phi + b, \tag{9}$$

where α_{Lu} is 0.27 for fine-textured soil and 0.96 for coarse-textured soil, a and b are empirical parameters and are determined to be 0.56 and 0.51 with ϕ being the porosity. Typically, the saturated (wet) conductivity is calculated via Johansen (1975):

$$\lambda_{wet} = \lambda_{solid}^{(1-\phi)} \times \lambda_w^{\phi}. \tag{10}$$

2.2.5 | Model domain

The dominant force at our test site in heat and water transport acts in the z-direction (from surface to ground). There is no force for a transport to occur in a horizontal direction. The zones corresponding to various porous media and land-use covers extend horizontally for short distances only (perpendicular to the pipes' length about 0.4 m, parallel to the pipes' length about 3 m) and are thermally insulated with polystyrene. Thus, boundary effects in horizontal directions are very small and can be neglected. For this reason, we chose

to represent the four stations of our setup (I, II, III, and IV) each with a 1D model without modeling the pipe of the test side. We worked with a daily resolution of the boundary conditions. For the different sections of the trench, there were layers in the solid materials modeled as seen in Figure 1. Each layer has its specific thermal and hydraulic properties. The covering layer was modeled as a separate layer for grass as well as for asphalt.

2.2.6 | Boundary conditions

The boundary condition at the bottom of the domain at the groundwater table was modeled as a Dirichlet boundary, which means, constant temperature and pressure were set. Temperature was set to the long-term groundwater average of 10°C; pressure was set to the equivalent of 0.9 m, which is the long-term water table at 5.1 m below ground surface. The boundary conditions at the ground surface for heat and water flow were set as Neumann boundary conditions, implying that both heat and water fluxes needed to be defined. To determine the flux values required for the Neumann condition, we computed heat and water balances at the interface.

Calculating Neumann conditions at the interface

The system behavior is driven by water and heat exchange with the atmosphere. We assume a constant temperature, as we reach lower soil layers, where conditions should be constant over time. Radiation and precipitation measured values of environmental influences, and the resulting heat and water fluxes need to be calculated to impose these influences as Neumann boundary conditions.

Heat

The balance of heat at the boundary can be written as:

$$\begin{aligned}\text{Soil heat flux} = {} & \text{Net radiation} - \text{Latent heat flux} \\ & - \text{Sensible heat flux} - \text{Heat flux due to net} \\ & \text{water flux.}\end{aligned} \tag{11}$$

The temperature of the infiltrating recharge as well as the contribution stemming from the evapotranspirating water is considered via the specific heat capacity of water and the temperature of air at 2 m height.

Incoming long and short wave radiation values are measured directly. Taking into account the albedo (ratio of incoming and outgoing short wave radiation; ω) of the surface and Boltzmann's law for outgoing long wave radiation, the resulting balance is:

$$\text{Net radiation} = H_{\text{short,in}} \times (1-\omega) + H_{\text{long,in}} - \sigma \times T_{\text{abs}}^4. \tag{12}$$

This equation can be directly solved, but latent and sensible heat fluxes cannot be directly calculated. Therefore, we use the so-called Bowen ratio:

$$\frac{\text{Sensible heat}}{\text{Latent heat}} = \frac{H_{\text{sens}}}{H_{\text{ET}}} = \gamma \times \frac{\frac{\partial \overline{T}}{\partial z}}{\frac{\partial \overline{e}}{\partial z}}. \tag{13}$$

The ratio of latent (H_{ET}) to sensible (H_{sens}) heat flux is equal to the ratio of the vertical gradients of temperature T with vapor pressure e multiplied by a constant, the so-called psychometric constant γ. This is based on the assumption of their similar turbulent diffusion coefficients. Now, we are approximating the gradients of e and T over a height z by the difference of their measured values at 2 m (e_{m} and T_{m}) and at surface (e_{surf} and T_{surf}). Then, we solve the equation by H_{ET}:

$$\frac{H_{\text{sens}}}{H_{\text{ET}}} = \gamma \times \frac{T_{\text{surf}} - T_{\text{m}}}{(e_{\text{surf}} - e_{\text{m}})} \rightarrow H_{\text{ET}} = \frac{(e_{\text{surf}} - e_{\text{m}}) \times H_{\text{sens}}}{(T_{\text{surf}} - T_{\text{m}}) \times \gamma}. \tag{14}$$

This gives us a relation for H_{sens} and H_{ET}, but does not define one of them. H_{ET} is defined as the heat flux at phase transition, this means latent heat of vaporization times density of water $\Delta H_{\text{vap}} \times \varrho_{\text{w}}$ times the rate of evapotranspiration ET:

$$H_{\text{ET}} = ET \times \Delta H_{vap} \times \varrho_{w} \tag{15}$$

To approximate ET, we use the Penman–Monteith equation, following Allen et al. (1998). Assuming a large surface of constant vegetation height, calculations based on boundary layer theory and Prandtl–Karman's velocity distribution lead to:

$$\begin{aligned} ET &= \frac{m_{\text{H}_2\text{O}}}{\varrho_{\text{w}} R T_{\text{abs}}} \frac{\kappa^2}{\left[\ln\left(\frac{z_{\text{m}} - t_{\text{d}}}{z_0}\right)\right]^2} u_{\text{m}} \times (e_{\text{surf}} - e_{\text{m}}) \\ &= \frac{m_{\text{H}_2\text{O}}}{\varrho_{\text{w}} R T_{\text{abs}} \times r_{\text{a}}} \times (e_{\text{surf}} - e_{\text{m}}), \end{aligned} \tag{16}$$

with the universal gas constant R, the von Karman constant κ the absolute temperature T_{abs} in K and r_{a} defined as

$$r_{\text{a}} = \frac{\left[\ln\left(\frac{z_{\text{m}} - t_{\text{d}}}{z_0}\right)\right]^2}{\kappa^2 \times u_{\text{m}}}, \tag{17}$$

which represents the aerodynamic resistance, $m_{\text{H}_2\text{O}}$ is the molar mass of water. Combining Equations (14)–(16), we end up with:

$$\begin{aligned} \frac{H_{\text{sens}}}{ET \times \Delta H_{\text{vap}} \times \varrho_{\text{w}}} &= \frac{H_{\text{sens}} \times R T_{\text{abs}} \times r_{\text{a}}}{m_{\text{H}_2\text{O}} \times \Delta H_{\text{vap}} \times (e_{\text{surf}} - e_{\text{m}})} \\ &= \frac{(T_{\text{surf}} - T_{\text{m}}) \times \gamma}{(e_{\text{surf}} - e_{\text{m}})}, \end{aligned} \tag{18}$$

Approximating r_a with $208/u_m$ (Allen et al., 1998), with the definition of the specific gas constant for air $R_s = R/m_{air}$, and $\epsilon = m_{H_2O}/m_{air}$ our boundary condition for H_{sens} results in:

$$H_{sens} = \frac{\epsilon \times \Delta H_{vap} \times \gamma}{T_{kv} \times R_s} \times \frac{u_m}{208} \times (T_{surf} - T_m), \quad (19)$$

T_{kv} is the virtual temperature, defined as $1.01 \times (T/°C + 273)$ (Allen et al., 1998).

The psychrometric constant γ is 66 Pa K^{-}1. As ET is defined as the evapotranspiration from a large surface of constant vegetation height, we need to consider the deviation from that idealized assumption at our site. To be pragmatic, we consider it as potential evapotranspiration and use a calibration factor f_{ET} to take into account the different surfaces as a property of the surface. Based on H_{sens}, we are now able to calculate H_{ET}, again using the Bowen ratio (Equation 14).

$$H_{ET} = f_{ET} \times \frac{\epsilon \times \Delta H_{vap}}{T_{kv} \times R_s} \times \frac{u_m}{208} \times (e_{surf} - e_m). \quad (20)$$

While the vapor pressure at ground surface, e_{surf}, is calculated via the Kelvin equation, the vapor pressure at 2 m, e_m, is determined from temperature T and humidity at 2 m, using the ideal gas law, directly in the simulation code.

Using Equations (20)–(12) we can now solve the heat balance (11) and assign meaningful boundary conditions.

Water

With ET defined in Equation (15), the water balance

$$\text{Incoming water} = \text{Precipitation - Evapotranspiration (ET)}, \quad (21)$$

can be solved as precipitation intensities were measured.

The basic balances are valid at the transition from air to soil. The asphalt cover can be described with its material parameters. For the land-use cover, we need to add an additional resistance, because the grass acts as an additional resistance. This resistance can be calculated as by Equation (19), but with the bulk surface resistance r_s instead of the aerodynamic resistance. The equation for the resistance λ of the grass cover is given below, where the value of r_s is set to 71 m s^{-}1 according to Allen et al. (1998).

$$\lambda = \frac{T_{kv} \times R_s}{\epsilon \times \Delta H_{vap} \times \gamma} \times r_s. \quad (22)$$

2.2.7 | Initial conditions

The system is sensitive to the initial conditions. Sensors were covering depths between 0.45 and 1.15 m, while values between 0 and 6 m were needed. Our initial approach was to interpolate the measured temperatures from 1.15 m below ground surface linearly down to the groundwater table (where the groundwater temperature is fixed to 10°C; see Section 2.2.6) and to assume a constant temperature between 0.45 m below ground surface and ground surface. This did not succeed, as we observed rising temperatures in lower layers at the beginning of calculation time, which seemed to have no physical reason. However, starting simulations with 1 year initialization period solved the problem, as shown in Figure S2. This fits to results presented in Yu et al. (2019), where the uncertainties of initial conditions are well documented.

2.2.8 | Calibration of the model

The required model parameters are known to different degrees and are associated with different uncertainties. As already indicated in the description of the boundary conditions above, some model parameters, such as permeability of the asphalt, must also assume "apparent" values due to the use of a 1D simplification, in order to integrate unconsidered multidimensional effects into the model through the back door, so to speak.

The properties of the fluids water (and air, though not modeled explicitly) are well known and their implementation in the model can be trusted. In particular the hydraulic properties in porous-media flow are usually associated with great uncertainty and variability. In this study, also the parameters for the thermal balance required attention since a sophisticated model was elaborated as explained above.

Some of the required parameters were measured, others are based on literature values (because measuring would have been too complicated). As the simulation time was short (approximately 20 min for one run), we calibrated parameters and finally arrived at parameter sets in good agreement with measurements. We note that the calibration was performed based on expert judgement without sophisticated algorithms or correlation analyses.

Assigning proper values to parameters for heat intake was difficult, as common databases such as Stephan et al. (2019) describe the material as one continuous solid at one fixed water saturation, not considering different saturations. In fact, in the partially saturated soil we encounter varying saturations and need to model property changes with saturation. Bertermann et al. (2018) give an overview on the change of soil properties based on their water contents. Farouki (1981) gives values for "pure" materials. These were used as average values for the parameter calibration for density, heat capacity, and solid thermal conductivity. The set of calibrated parameters, which we finally used as well as their values of variation are listed in Table 1. The capillary pressure–saturation curves for

TABLE 1 Overview over parameter values used in simulations.

(a) Parameters for heat transport.				
	λ		c_p	
Material	**Varied range**	**End value**	**Varied range**	**End value**
Asphalt	0.7–1	1	600–800	700
Grass	3–9	5	600–800	800
Sand	2.5–7	5	600–900	600
Gravel coarse	2.5–9	5	600–800	800
Gravel sieved	2.5–9	5	600–800	800
Natural material	2.5–9	3	600–800	732
Lower material	2.5–9	5	600–800	732

(b) Parameters for water transport where "VG" stands for van Genuchten.					
	Permeability in 1 m^2	**Porosity**		**VG: α**	**VG: n**
Material	**Value**	**Varied range**	**End value**	**value**	**value**
Asphalt	1.46e−10	-	0.3	18.395	1.2
Clay	9.45e−12	Measured	0.533	18.395	1.301
Lower material	1.1e−11	0.3–0.533	0.4	15	1.1
Gravel coarse	6.65e−12	0.3–0.4	0.36	2	1.5
Gravel sieved	9.3e−12	0.3–0.4	0.3	2	1.5
Grass	6.65e−12	0.3–0.4	0.36	2	1.45
Sand	9.3e−12	0.3–0.4	0.36	15	1.3

(c) Parameters for forcing function at ground surface.				
	f_{ET}		**albedo**	
Material	**Varied range**	**End value**	**Varied range**	**End value**
Grass	0.4–0.6	0.6	0.18–0.26	0.26
Asphalt	0.6–0.8	0.8	0.12–0.15	0.15

the porous media at the pilot site with final calibrated values of Table 1 are shown in Figure S3.

The temperature in the topmost region is highly sensitive to the fitting parameter for evapotranspiration, f_{ET}, and the albedo value ω, while transport parameters become relevant further below. Based on that, we first fitted f_{ET} and ω to the temperature measurements in the topmost 30 cm, upon which heat transport parameters were varied, that is, heat conductivity and heat capacity. Parameters with high sensitivity include the permeability, the moisture content, which is closely coupled to porosity. The used set of parameters can be found in Table 1).

3 | RESULTS

3.1 | Measured data

The results of the measurements, which we interpret as the meteorological forcing functions for the temperature evolution in the different stations of our experimental pilot site are given in Figure 2. They include (from top to bottom) long wave and short wave radiation, the temperature at a height of 2 m above ground, the wind velocity at 2 m height, the air humidity, and the precipitation. The data show the transition from the summer (i.e, August 2020) to the winter (i.e., December 2020) with associated trends of decreasing temperatures and radiation intensities as well as increasing air humidity.

Figure 3 shows the temperature time series for the four stations at the experimental pilot site separated into individual panels for discrete vertical depths. Gaps in the bottom panel indicate missing data. The land-use cover at Stations I and IV is natural vegetation (grass), while it is asphalt at Stations II and III. The subsurface material is naturally occurring silty clay at Stations I and II, and is gravelly material at Stations III and IV. The data show that the type of land-use cover has a larger influence on the evolution of subsurface temperatures than the porous material in the subsurface at our pilot site. This is indicated by small temperature differences between the green curves and the grey curves in Figure 3.

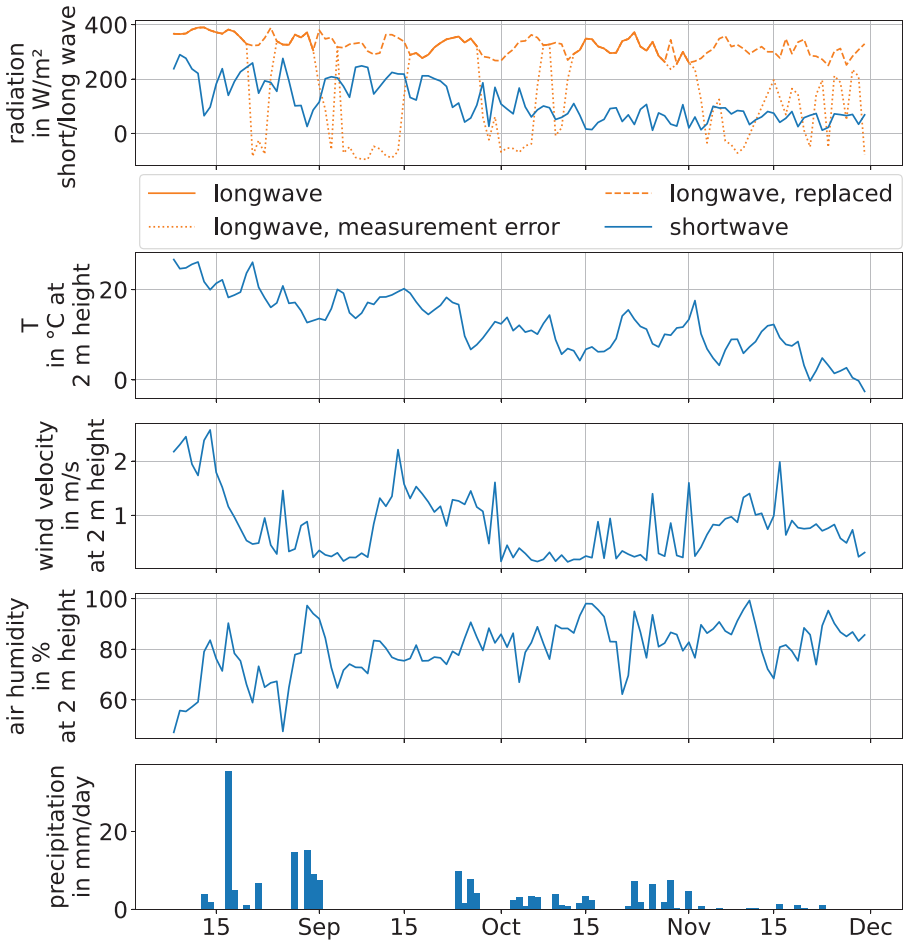

FIGURE 2 Meteorological forcing functions: Data from the nearby weather station.

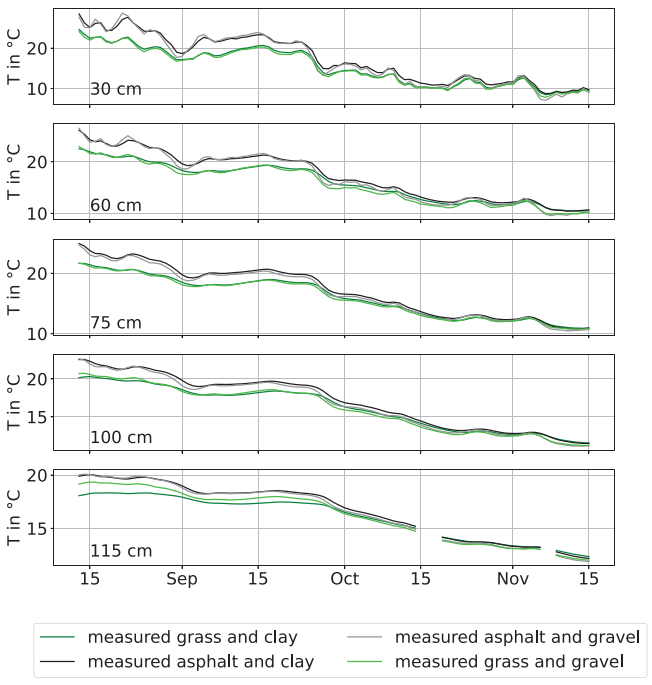

FIGURE 3 All measured soil temperatures over time.

3.2 | The match between measurements and numerical model

The main results of this study is the calibration of the numerical model to the measured data, which is presented below.

Figure 4 shows two subplots of subsurface temperature evolutions during a time period in September 2020 at the four stations. Subplot (a) contains the measured temperatures and in comparison to that there is subplot (b) with the calibrated corresponding numerical simulation results. From (a), the dynamics in the evolution of the vertical temperature profiles is visible. The color coding indicates the time from September 1 (purple) to September 21 (yellow). A larger spatial spread can be observed in this figure's central panels (Stations II and III), which represent the asphalt land-use, than in the most left and most right panel (Stations I and IV), which are both with grass as land-use. This indicates that, at least for this design of the experiments, the type of land-use has a stronger influence on temperature evolution than the soil properties. The asphalt-covered gravel section (Station III) spreads even more than the corresponding natural material

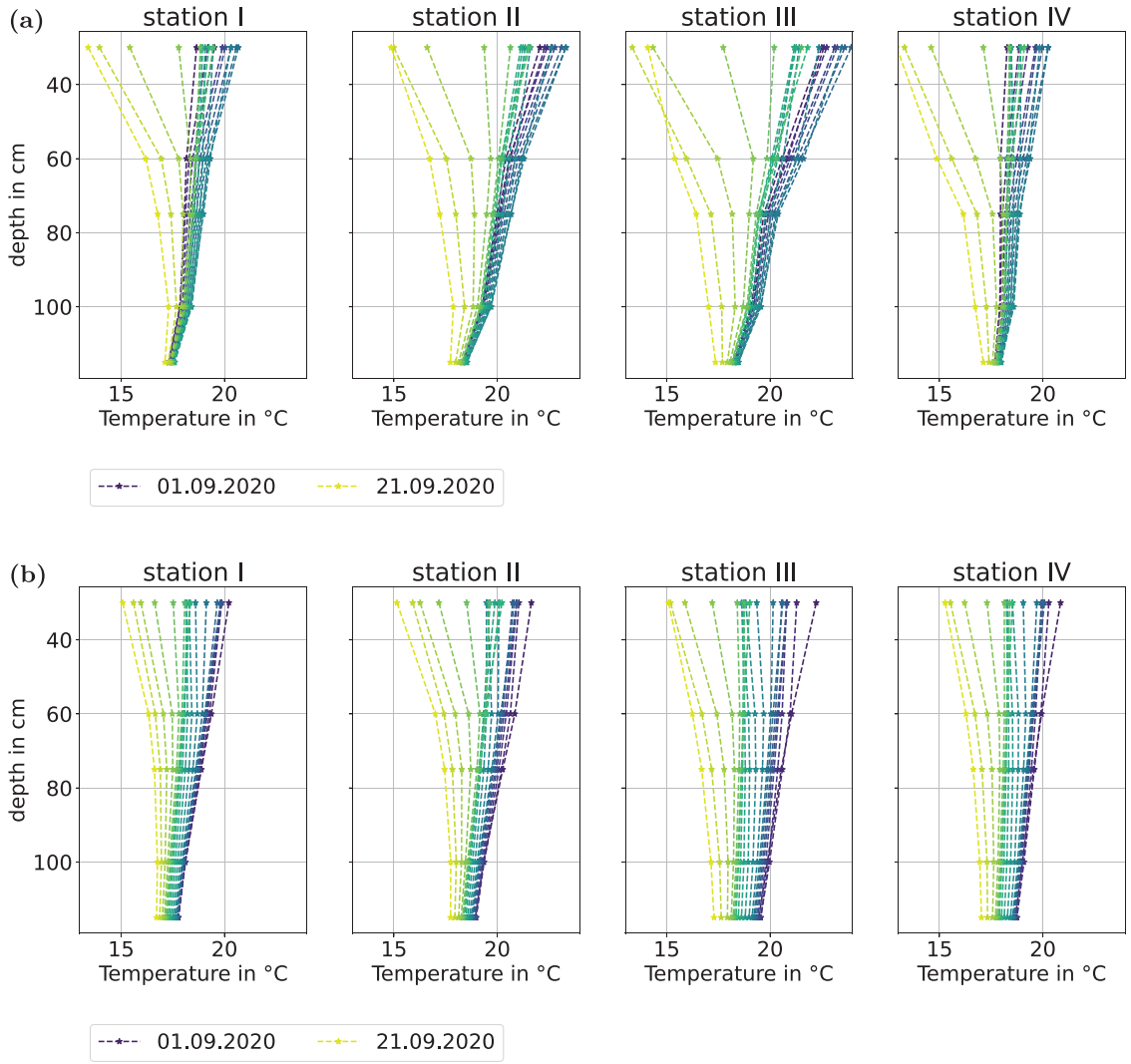

FIGURE 4 Evolution of temperature profiles in the subsurface. (a) Temperature over depth for several days, *measured*, (b) Temperature over depth for several days, *simulated*. Legend dates are dd.mm.yyyy.

underneath (Station IV), which proves that there is certainly also an effect due to the different layers below the top cover. Generally, the model is able to reproduce measured soil moisture dynamics at various depths and under various land-use as well.

Figure 4 contrasts precipitation data (top panel) with both measured and simulated water saturations in two different depths, that is, at 60 cm (middle panel) and at 100 cm (bottom subplot). The different stations I–IV are represented in the curves according to their labeling in the legend with grass or asphalt as covers and natural material or gravel underneath underneath. Easy to remember, green curves represent grass land-use and, accordingly, black represents asphalt. Dashed lines indicate simulated curves. Our calibrated model (panel b) is able to reproduce the larger temperature spread under asphalt than under grass with depth and its temporal evolution very similarly at the observations (panel a). The influence of precipitation in the curves observed in the experiments at the pilot site is smaller at deeper regions. Relatively small precipitation events, even where they occur over multiple consecutive days (e.g., during October 2020) are not detected in the saturation data. In contrast to that, the simulated curves show the impact of precipitation on water saturation, that is, soil moisture, is more finely nuanced.

Overall, during the period from August until December 2020, subsurface temperatures decline as expected following the trend of declining seasonal average temperatures in the fall. The deeper below ground surface the more are the amplitudes of temperature fluctuations attenuated. Figure 6 shows how the calibrated model reproduces the observed temperatures in good qualitative agreement; the accuracy of the match between calibrated model and observation tends to be better in the deeper regions close to the drinking-water pipes. The curves for the natural material underneath with asphalt/grass on top (Stations I/II) is plotted on the left, accordingly Stations III/IV with gravel underneath are seen on the right. Asphalt cover is plotted in black and grass cover in green.

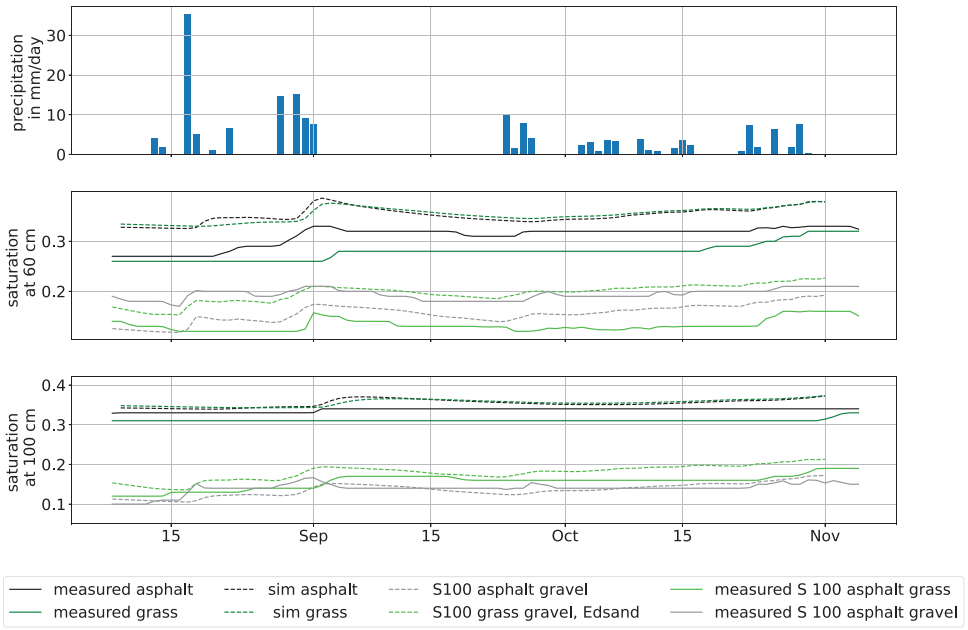

FIGURE 5 Precipitation data and corresponding measured versus simulated saturations over time. Dashed lines show simulated curves.

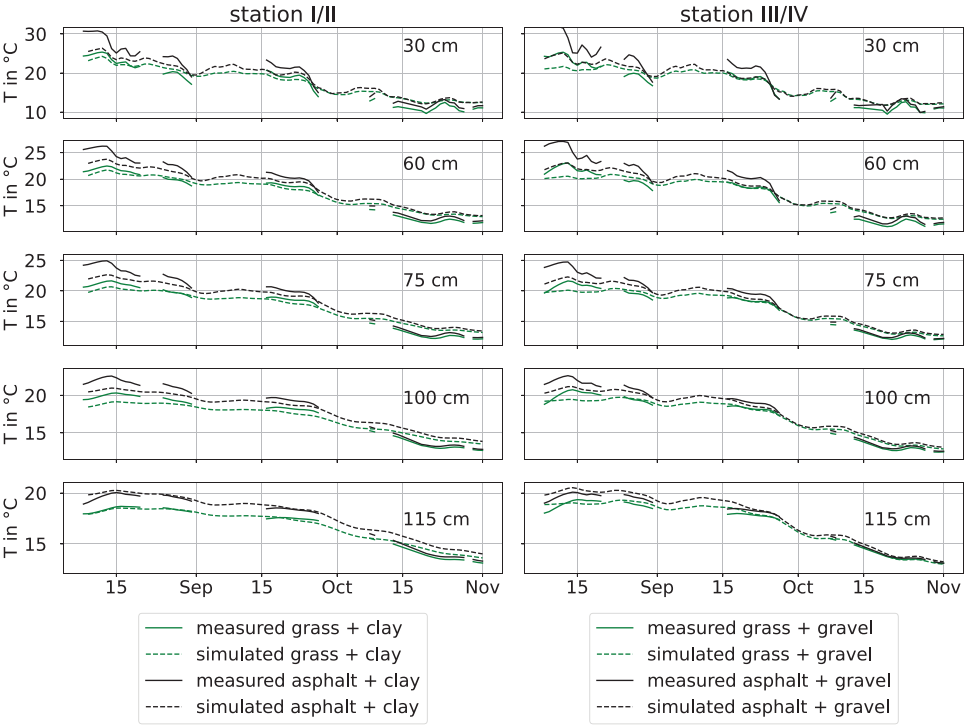

FIGURE 6 Simulated (after calibration) and measured temperatures at different depths versus time for all stations.

The amplitudes of temperatures at the interface between soil and the meteorological are dampened with increasing depth and are not detectable anymore at a depth of 115 cm. Up to depths of about about 1 m, the short-term high temperature amplitudes are dampened and occur at the pilot site with a delay of about 1 to 2.5 days.

There is a noticeable mismatch between measured and simulated curves for the asphalt cover at the very early times, which can be attributed to the still hot asphalt after its pouring. This mismatch diminishes by early September. The periods where the temperature data is not plotted continuously, gaps marks those time periods where there are no correct

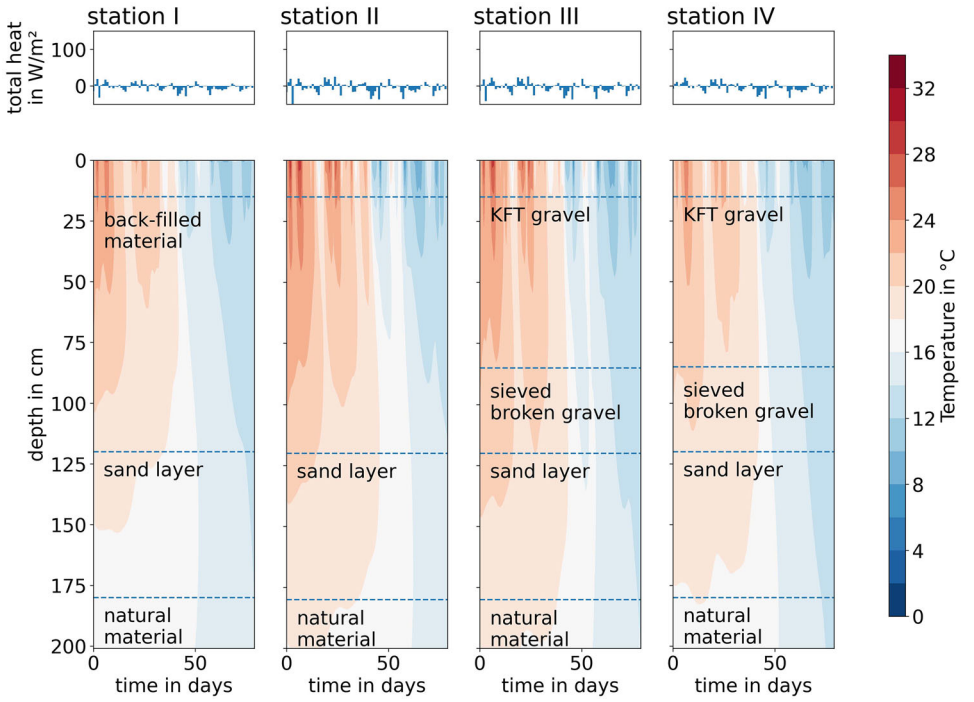

FIGURE 7 Soil temperatures plotted over time and height with total heat as forcing function (top panels).

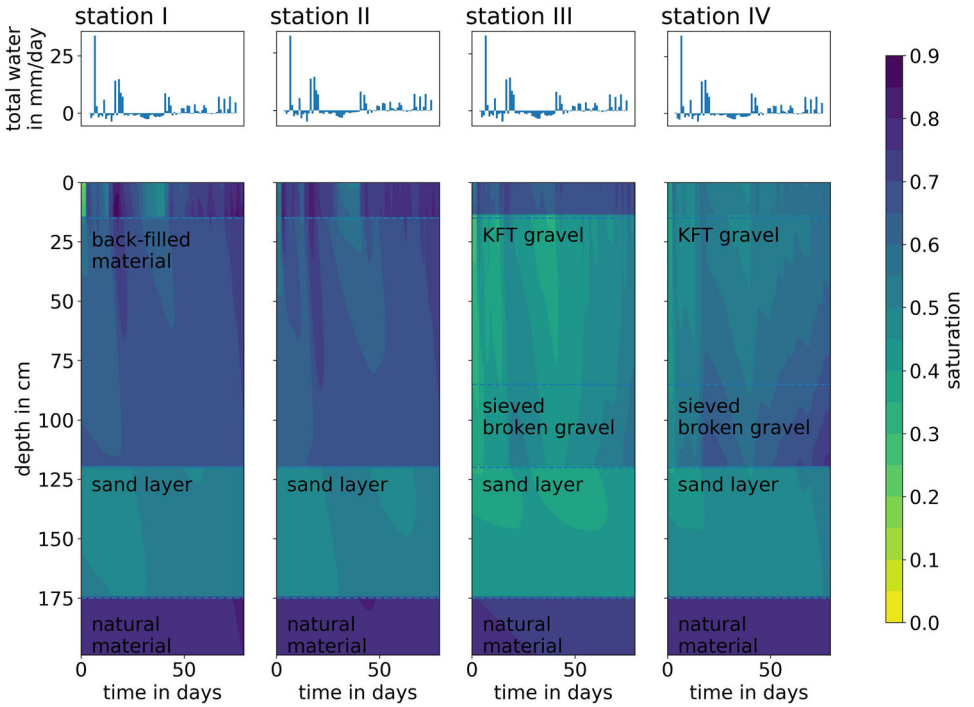

FIGURE 8 Contour plots of water saturations over time in the soil with total water influx as forcing function.

boundary conditions available, particularly due to the erroneous long wave sensor. To be able to feed the model with required boundary conditions, we used the long-wave data of the year 2015, which exhibited similar statistical moments in those periods. Obviously, the simulated temperatures mostly follow the measured trends, but start with a bigger difference after periods with missing "correct" radiation data. Looking at absolute temperature differences, we notice that they are smaller than ≈8 K in the beginning at higher positions, while at lower positions they are below 1 K. The temporal

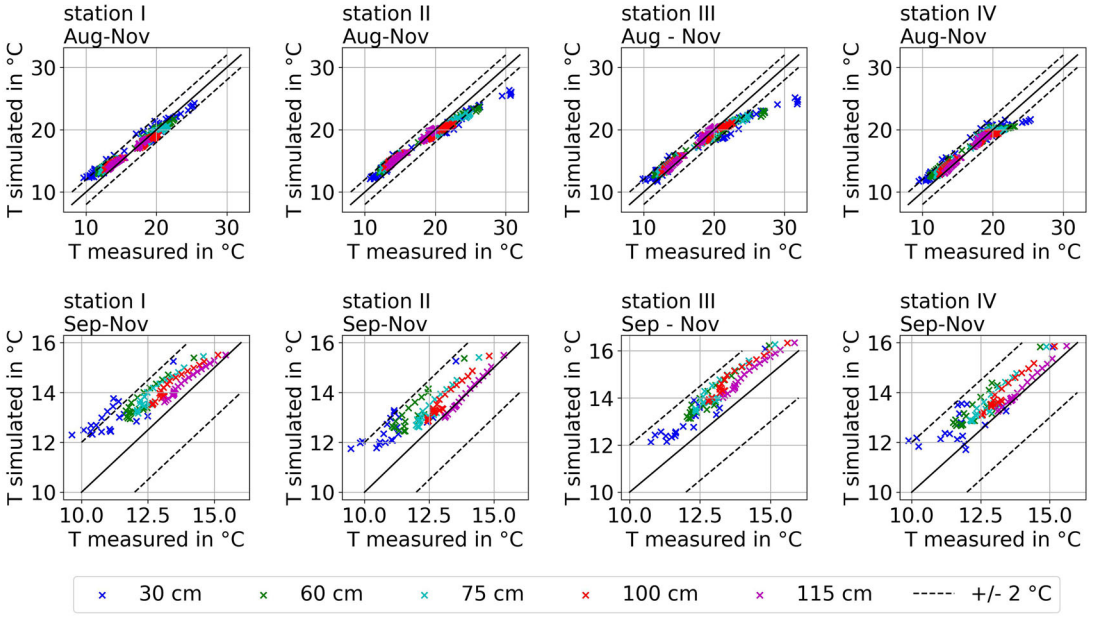

FIGURE 9 Performance plots of measured versus simulated temperatures. Top panels for entire time series, bottom panels for a smaller temperature range exclude the early time when the temperatures were still biased by freshly installed asphalt.

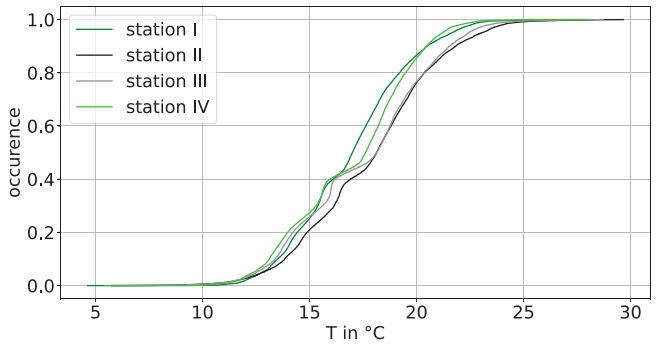

FIGURE 10 Standardized cumulative frequency of simulated temperatures.

evolution of temperature differences between measurements and observations is shown in Figure S6.

Figures 7 and 8 are intended to give an impression of the dynamics of heat and moisture transport in the soil body as obtained from the numerical model. At the top of these time-map illustrations, we provide the meteorological forcing functions, that is, total heat and total water, respectively. The heat forcing is reflected directly by the temperature response in the model domain. Comparing Stations I and IV (both grass cover, but with different layers underneath), we observe a difference in the temperature distributions: in gravel, the extents of zones of elevated temperatures are larger with smaller gradients. The gravel systems, as expected, react faster than the clayey zones. This difference in heat transport dynamics is smaller for Stations II and III (with asphalt). Regarding the soil moisture dynamics as expressed by the time maps of water saturation in Figure 8, we can see that the gravel layer acts as an efficient drainage (green zones). While there is no strong difference in soil moisture dynamics between asphalt and grass cover for the back-filled material, the gravel and grass cover combination tends to lead to a drier soil body.

Focusing on the difference of the stations, all simulated temperatures were summed and plotted as standardized cumulative frequency of T in Figure 10. Grass-covered stations (green lines) are to the left of the other lines in this plot, which indicates that grass-covered regions have a tendency to be colder. In the range of to 20°C, there are differences in slope, which means that the difference of temperatures is not always the same. The type of land-use cover plays an even more important role during hot days (Figure S7).

We conclude this results section with a detailed quantitative assessment of the match between measured and simulated temperatures as given by Figure 9. The performance plot analyses the deviations between model and experiment for different depth zones. The top row considers the entire time period, while in the bottom row the first month was left out. It was mentioned already above that we expect here a bias due to freshly poured asphalt and, thus, elevated temperatures which are not due to meteorological forcing functions. The model can reproduce the trends of the measured data, that is, the order of temperatures, higher temperature spreading under asphalt cover. The match between model results and observation data is generally good, while the deviations vary in a range of ~±2 K for the entire period (upper panels). When excluding the first month from this analysis, the performance is always better than ±2 K, while a small consistent overestimation (~+2 K) by the model can be noticed.

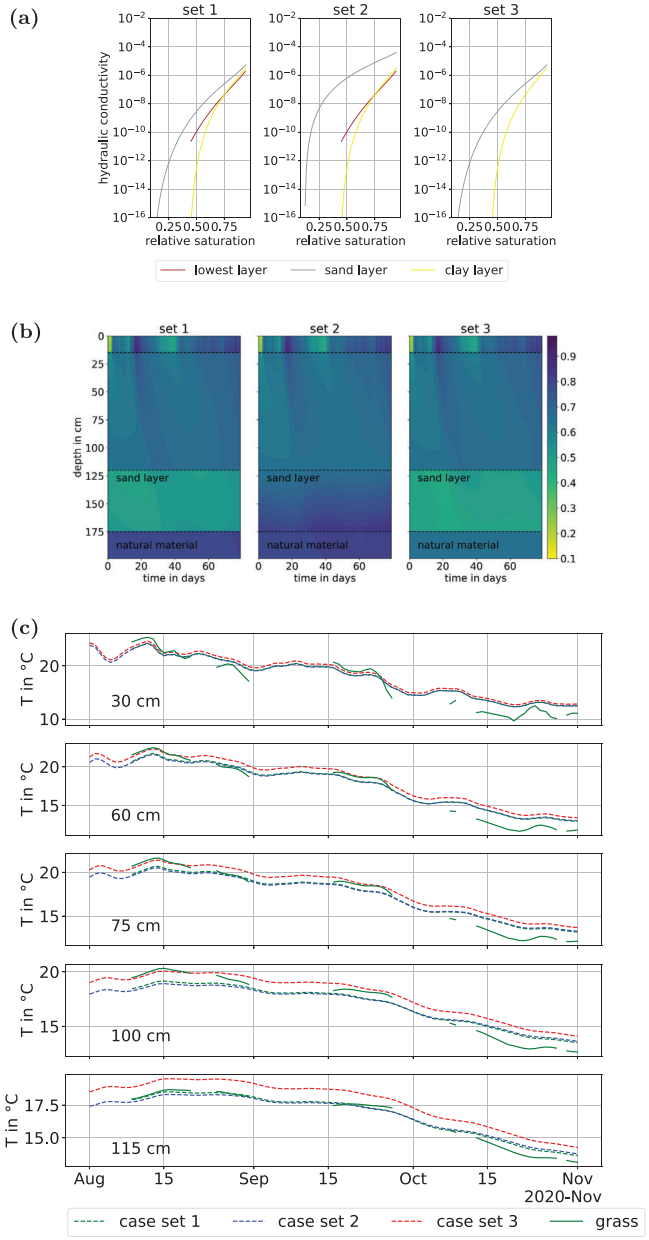

FIGURE 11 Evaluating the effect of the variably-saturated material properties. (a) Three sets of possible capillary pressuresaturation relationships, (b) Simulated saturations (contoured over depth and time) for the different sets, (c) Simulated temperatures at various depths for the different sets.

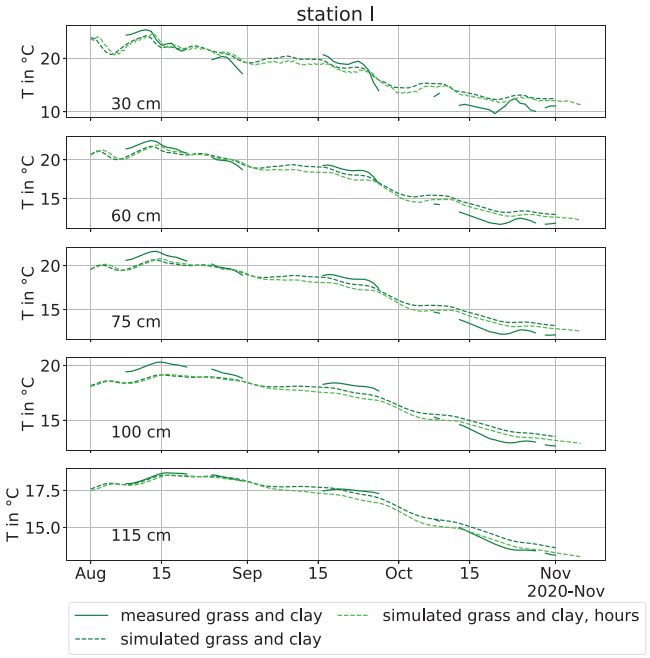

FIGURE 12 Comparison of time series of simulated and measured temperatures with varying temporal resolution in input data.

4 | DISCUSSION

4.1 | The agreement between measurement and simulation (part A)

The results show, as summarized, for example, in Figure 9, that calibrated numerical simulations are in satisfactory, partly even excellent agreement with the measured data. Thus, we can claim with confidence that the model is able to not only qualitatively, but also quantitatively is able to describe on a seasonal time scale the governing physical processes that lead to temperature evolution in the depths of drinking-water pipes as driven by meteorological forcing functions in terms of temperature curves and precipitation data. We note that the calibration was not globally optimized and no correlation metrics were calculated. For example, the simulated results are sensitive to the van Genuchten parameters for relative permeability and capillary pressure. We have tested several sets of parameters and evaluated them with respect to best fitting the measured data. We have found that for the overall match between data and simulation, it is in particular important to match saturations in the lowest and topmost regions and to adapt the van Genuchten parameters accordingly, as shown in Figure 11a.

4.2 | The agreement between measurement and simulation (part B)

The calibrated 1D model had to cope with some effects that are obviously multidimensional, which inevitably means that the calibrated parameter values are not in all instances the "real" values. For example, the asphalt cover is ideally close to impermeable, while there has been some small amount of water infiltrating from laterally, see also the discussion on boundary conditions.

4.3 | On initial conditions

Furthermore, the difficulties with a good set of initial conditions has been mentioned, which was addressed here with

a simulated initialization period. The materials were back-filled into the trench and had to equilibrate with ambient conditions for some time. It is also important to note that the measurements started while the asphalt still was fresh and the temperatures were still elevated for a couple of days. This explains why the agreement between simulation results and measurements improves at later time periods.

4.4 | On the influence of the boundary conditions

Grass is not sufficiently homogeneous for practical measurements of variably saturated parameters and asphalt is not permeable. Water intrusion does not occur through the asphalt layer itself, but, since it has limited lateral extent, from the sides, so that the situation modeled as 1D must in reality be considered at least 2D. Thus, the material underneath the asphalt is in fact not completely dry, which means, that a representative set of variably saturated parameter values at the top boundary had to be found in order to cope with that situation. Alternatively, the system had to be modeled in 2D, which would have increased computational costs tremendously. Instead of that, we were fitting van Genuchten parameters and permeability such that the resulting saturation fitted to observations.

The boundary conditions in the 1D system strongly affect the moisture distribution in the porous media. The two coarse layers transport all water faster. For achieving a good fit in saturation, it is important to work with values, which have at all times a better conductivity than sand. Parameter studies also showed that the natural material below the test side needs to have saturation values that are different from those of the back-filled material. As the deeper material was not manipulated and might also change in greater depths, this seems reasonable.

4.5 | On the length of simulation period

We modeled only the cooling phase, as other values were not available, when we started. This leaves the possibility, a calibration would have led to different parameters with a longer period. For this reason, we are at the moment working on longer time periods.

4.6 | On the heat balance solved in this application

The solution of the heat balance coupled to the moisture transport employs a novel and sophisticated approach to consider the soil–atmosphere interface. This involves a number of parameters, which need to be determined, partly based on idealized assumptions, which may not be given as ideal as assumed. This concerns in particular the assumption of a large surface of constant vegetation height, as required for calculating the evapotranspiration, see Equation (16). In order to have a tool to adapt the assumption to the reality, we introduced a calibration parameter, f_{ET}. Thus, one might question the approach with respect to possible over-parameterization or over-sophistication for such a small surface as we have it in our application. On the other hand, the coupled, calibrated solution, gave very satisfactory agreement and the model helps including meteorological parameters to foster the better understanding of processes and parameters, which is considered as important as the reliable prediction of temperatures.

In addition, such sophisticated models require reliable meteorological time series over long periods. As our study showed, sometimes sensors fail and backup sensors, double measurements, etc. would be useful.

4.7 | On the temporal resolution of the data as input for the modeling

Regarding the temporal resolution of the measured data in the numerical model, we note that a daily precipitation time series was chosen instead of the available hourly series. The reason for that is that the daily series is more smooth and does not force the model to resolve sudden high peak values, which led to very strong changes in saturation, in particular for the gravel. Relative to the observation time, we assume that a daily average does not introduce significant errors in water content distribution over depth, as can be seen in Figure 12.

5 | CONCLUSIONS

The transient dynamics of water saturation and temperatures in the shallow subsurface, dependent on land-use cover and back-fill material were modeled with quite some confidence when meteorological data are available. Beyond this study, the prediction of seepage water temperatures has relevance for further applications as in geothermal heating/cooling systems especially in urban environments. The influence of heat balances coupled to water transport, thus including also evapotranspiration, is in particular high due to the water's very high latent heat of vaporization.

The land-use cover has the biggest effect both on temperatures and saturations in the subsurface, while the soil structure is also relevant, but not as much.

Good initial data at all depths have proven to be crucial. They need to be either known and if (partially) missing be obtained by an initialization period in the model to allow

for the conditions in the layer to adapt to meteorological data.

To achieve a good quality of predicted temperature distribution, it is important to have correct saturation data. The model reacts sensitively on saturation parameters and radiation data, while density, heat capacity, and thermal conductivity are more robust.

More calibration and validation efforts are needed. We plan to calibrate also the spring season, where temperatures tend to increase, and thus to further increase the confidence in the model. This will allow for modeling climate-change scenarios to derive suggestions for resilient design criteria for drinking-water supply networks.

AUTHOR CONTRIBUTIONS

Elisabeth Nissler: Conceptualization; formal analysis; data curation; investigation; writing—original draft; visualisation. **Samuel Scherrer**: Conceptualization; methodology development; software. **Holger Class**: Conceptualization; methodology; writing—review and editing. **Tanja Müller**: Pilot site construction; investigation; resources; data curation. **Mark Hermannspan**: Pilot site construction; investigation; resources; data curation. **Esad Osmancevic**: Conceptualization; methodology; resources; writing—review and editing; funding acquisition. **Claus Haslauer**: Conceptualization; methodology; resources; writing—review and editing; supervision; project administration; funding acquisition.

ACKNOWLEDGMENTS

We thank Radhakrishna Bangalore Lakshmiprasad for his tireless efforts during the establishment of the pilot site. We also thank Oliver Trötschler, Henning Eickhoff, Marko Schmitt, Alexander Bässler, and Steffen Hägele for their technical and humorous support. Special thanks to Oliver Trötschler for his expertise as an operating engineer, to Ramona Häckl for her versatile support, and all colleagues in the coffee corner. We also thank the public services department of the city of Sindelfingen ("Stadtwerke Sindelfingen") for their technical support.

CONFLICT OF INTEREST STATEMENT

The authors declare no conflicts of interest.

DATA AVAILABILITY STATEMENT

At publication time the code and the data will be made available as a FAIR (https://www.izus.uni-stuttgart.de/en/fokus/darus/) DaRUS repository. The code and its results are in the dataset (https://darus.uni-stuttgart.de/dataset.xhtml?persistentId=doi:10.18419/darus-3552) DockerContainer, where dumux can be run via a docker-container and the results are documented for the four stations as tabulated values. Data, used for Boundary Conditions is available at (https://darus.uni-stuttgart.de/dataset.xhtml?persistentId=doi:10.18419/darus-3554) Meteorologic data, while measured soil moisture and temperature data, used for validation is to be found at (https://darus.uni-stuttgart.de/dataset.xhtml?persistentId=doi:10.18419/darus-3555) Soil Data.

ORCID

Claus Haslauer https://orcid.org/0000-0003-0180-8602

REFERENCES

Allen, R., Pereira, L., Raes, D., & Smith, M. (1998). Chapter 2–fao penman-monteith equation. *Crop evapotranspiration–Guidelines for computing crop water requirements* (Irrigation and Drainage Paper no. 56). https://www.fao.org/3/X0490E/x0490e00.htm

Bertermann, D., Müller, J., Freitag, S., & Schwarz, H. (2018). Comparison between measured and calculated thermal conductivities within different grain size classes and their related depth ranges. *Soil Systems*, *2*, 50.

Bittelli, M., Ventura, F., Campbell, G. S., Snyder, R. L., Gallegati, F., & Pisa, P. R. (2008). Coupling of heat, water vapor, and liquid water fluxes to compute evaporation in bare soils. *Journal of Hydrology*, *362*(3-4), 191–205.

Brooks, R. H., & Corey, A. T. (1966). Properties of porous media affecting fluid flow. *Journal of the Irrigation and Drainage Division*, *92*(2), 61–88.

Chen, L., Aalto, J., & Luoto, M. (2021). Decadal changes in soil and atmosphere temperature differences linked with environment shifts over northern eurasia. *Journal of Geophysical Research: Earth Surface*, *126*(3), e2020JF005865.

Clapp, R. B., & Hornberger, G. M. (1978). Empirical equations for some soil hydraulic properties. *Water Resources Research*, *14*(4), 601–604.

Corona, C. R., & Ge, S. (2022). Examining subsurface response to an extreme precipitation event using HYDRUS-1D. *Vadose Zone Journal*, *21*, e20189. https://doi.org/10.1002/vzj2.20189

Farouki, O. (1981). *Thermal properties of soils. U.S. Army Corps of Engineers, Cold Regions Research and Engineering Laboratory*.

Ghanbarian, B., & Daigle, H. (2015). Thermal conductivity in porous media: Percolation-based effective-medium approximation *Water Resources Research*, *52*, 295–314. https://doi.org/10.1002/2015WR017236

Guo, J., Blankenburg, R., Geng, X., & Graeber, P.-W. (2017). Hydrological process analysis in earth dams using the pcsiwapro® as a basis for stability analysis. *Journal of Geological Resource and Engineering*, *3*, 139–145. https://doi.org/10.17265/2328-2193/2017.03.004

Herrada, M. A., Gutiérrez-Martin, A., & Montanero, J. M. (2014). Modeling infiltration rates in a saturated/unsaturated soil under the free draining condition. *Journal of Hydrology*, *515*, 10–15.

Horton, B., & Corkrey, R. (2011). A weighted coefficient model for estimation of Australian daily soil temperature at depths of 5 cm to 100 cm based on air temperature and rainfall. *Soil Research*, *49*, 305–314. https://doi.org/10.1071/SR10151

Idrissou, M., Diekkrueger, B., Tischbein, B., Ibrahim, B., Yacouba, Y., Steup, G., & Pomeon, T. (2020). Testing the robustness of a physically-based hydrological model in two data limited inland valley catchments in dano, burkina faso. *Hydrology*, *7*, 43.

Johansen, O. (1975). *Thermal conductivity of soils* [Ph.D. thesis]. Institute for Cold Technology Trondheim.

Jungqvist, G., Oni, S., Teutschbein, C., & Futter, M. (2014). Effect of climate change on soil temperature in swedish boreal forests. *PloS One*, *9*, e93957.

Kelleners, T. J., Koonce, J., Shillito, R., Dijkema, J., Berli, M., Young, M. H., Frank, J. M., & Massman, W. (2016). Numerical modeling of coupled water flow and heat transport in soil and snow. *Soil Science Society of America Journal*, *80*(2), 247–263. https://doi.org/10.2136/sssaj2015.07.0279

Koch, T., Glaeser, D., Weishaupt, K., Ackermann, S., Beck, M., Becker, B., Burbulla, S., Class, H., Coltman, E., Emmert, S., Fetzer, T., Grueninger, C., Heck, K., Hommel, J., Kurz, T., Lipp, M., Mohammadi, F., Scherrer, S., Schneider, M., … Flemisch, B. (2020). Dumu^{x} 3 - An open-source simulator for solving flow and transport problems in porous media with a focus on model coupling. *Computers & Mathematics with Applications*, *81*, 423–443. https://doi.org/10.1016/j.camwa.2020.02.012

Komolvilas, V., & Kikumoto, M. (2017). Simulation of liquefaction of unsaturated soil using critical state soil model. *International Journal for Numerical and Analytical Methods in Geomechanics*, *41*(10), 1217–1246.

Kurylyk, B. L., Macquarrie, K. T. B., Caissie, D., & Mckenzie, J. M. (2015). Shallow groundwater thermal sensitivity to climate change and land cover disturbances: derivation of analytical expressions and implications for stream temperature modeling. *Hydrology and Earth System Sciences*, *19*(5), 2469–2489.

Lu, N., & Dong, Y. (2015). Closed-form equation for thermal conductivity of unsaturated soils at room temperature. *Journal of Geotechnical and Geoenvironmental Engineering*, *141*, 04015016.

Lu, S., Ren, T., Gong, Y., & Horton, R. (2007). An improved model for predicting soil thermal conductivity from water content at room temperature. *Soil Science Society of America Journal*, *71*(1), 8–14. https://doi.org/10.2136/sssaj2006.0041

Markert, A., Bohne, K., a, M., & Wessolek, G. (2017). Pedotransfer functions of soil thermal conductivity for the textural classes sand, silt and loam. *Soil Science Society of America Journal*, *81*, 1315–1327. https://doi.org/10.2136/sssaj2017.02.0062

Osmancevic, E., & Hüsam, S. (2021). Einfluss des Klimawandels auf die Trinkwasserversorgung in Süddeutschland. *gwf Wasser und Abwasser*. https://gwf-wasser.de/produkt/einfluss-des-klimawandels-auf-die-trinkwasserversorgung-in-sueddeutschland/

Peters, A., & Durner, W. (2008). Simplified evaporation method for determining soil hydraulic properties. *Journal of Hydrology*, *356*(1), 147–162.

Rankinen, K., Karvonen, T., & Butterfield, D. (2004). A simple model for predicting soil temperature in snow-covered and seasonally frozen soil: Model description and testing. *Hydrology and Earth System Sciences*, *8*, 706–716.

Sadeghi, M., Ghanbarian, B., & Horton, R. (2018). Derivation of an explicit form of the percolation-based effective-medium approximation for thermal conductivity of partially saturated soils. *Water Resources Research*, *54*, 1389–1399.

Saito, H., Šimůnek, J., & Mohanty, B. P. (2006). Numerical analysis of coupled water, vapor, and heat transport in the vadose zone. *Vadose Zone Journal*, *5*(2), 784–800. https://doi.org/10.2136/vzj2006.0007

Sandor, R., & Fodor, N. (2012). Simulation of soil temperature dynamics with models using different concepts. *The Scientific World Journal*, *2012*, 590287.

Scheer, D., Class, H., & Flemisch, B. (2020). *Subsurface environmental modelling between science and policy*. Springer Cham. https://doi.org/10.1007/978-3-030-51178-4

Sharma, P., Shukla, M., & Sammis, T. (2010). Predicting soil temperature using air temperature and soil, crop, and meteorological parameters for three specialty crops in southern new mexico. *Applied Engineering in Agriculture*, *26*, 47–58.

Simunek Jiri, J., & Bradford, S. (2008). Vadose zone modeling: Introduction and importance. *Vadose Zone Journal*, *7*, 581–586. https://doi.org/10.2136/vzj2008.0012

Somerton, W., El-Shaarani, A., & Mobarak, S. (1974, April 4–5). *High temperature behavior of rocks associated with geothermal type reservoirs* [Paper presentation]. SPE California Regional Meeting, San Francisco, CA. https://doi.org/10.2118/4897-MS

Steenpass, C., Vanderborght, J., Herbst, M., Šimůnek, J., & Vereecken, H. (2010). Estimating soil hydraulic properties from infrared measurements of soil surface temperatures and TDR data. *Vadose Zone Journal*, *9*(4), 910–924. https://doi.org/10.2136/vzj2009.0176

Stephan, P., Kabelac, S., Kind, M., Mewes, D., Schaber, K., & Wetzel, T. (Eds.). (2019). *VDI-Wärmeatlas*. Springer.

Tran, A. P., Dafflon, B., Hubbard, S. S., Kowalsky, M. B., Long, P., Tokunaga, T. K., & Williams, K. H. (2016). Quantifying shallow subsurface water and heat dynamics using coupled hydrological-thermal-geophysical inversion. *Hydrology and Earth System Sciences*, *20*(9), 3477–3491.

Virtanen, P., Gommers, R., Oliphant, T. E., Haberland, M., Reddy, T., Cournapeau, D., Burovski, E., Peterson, P., Weckesser, W., Bright, J., van der Walt, S. J., Brett, M., Wilson, J., Millman, K. J., Mayorov, N., Nelson, A. R. J., Jones, E., Kern, R., Larson, E., … van Mulbregt, P. (2020). SciPy 1.0: Fundamental algorithms for scientific computing in Python. *Nature Methods*, *17*, 261–272.

Wang, Z.-H. (2012). Reconstruction of soil thermal field from a single depth measurement. *Journal of Hydrology*, *464-465*, 541–549.

Wessolek, G., Bohne, K., Trinks, S., & Kluge, B. (2022). Case studies on soil heating by cables liners. *Journal of Modern and Applied Physics*, *5*, 1–6.

Yang, J., & Wang, Z.-H. (2014). Physical parameterization and sensitivity of urban hydrological models: Application to green roof systems. *Building and Environment*, *75*, 250–263.

Yu, D., Yang, J., Shi, L., Zhang, Q., Huang, K., Fang, Y., & Zha, Y. (2019). On the uncertainty of initial condition and initialization approaches in variably saturated flow modeling. *Hydrology and Earth System Sciences*, *23*(7), 2897–2914.

SUPPORTING INFORMATION

Additional supporting information can be found online in the Supporting Information section at the end of this article.

How to cite this article: Nissler, E., Scherrer, S., Class, H., Müller, T., Hermannspan, M., Osmancevic, E., & Haslauer, C. (2023). Heat transport from atmosphere through the subsurface to drinking-water supply pipes. *Vadose Zone Journal*, *22,* e20286. https://doi.org/10.1002/vzj2.20286